Supplementary Information for "High-temperature phonon-mediated superconductivity in monolayer $Mg_2B_4C_2$"

Sobhit Singh,[1,*] Aldo H. Romero,[2,†] José D. Mella,[3,4] Vitalie Eremeev,[5] Enrique Muñoz,[6] Anastassia N. Alexandrova,[7,8] Karin M. Rabe,[1] David Vanderbilt,[1] and Francisco Muñoz[4,9,‡]

[1]*Department of Physics and Astronomy, Rutgers University, Piscataway, New Jersey 08854, USA*

[2]*Department of Physics and Astronomy, West Virginia University, Morgantown, West Virginia 26506, USA*

[3]*Departamento de Física, Facultad de Ciencias Físicas y Matemáticas, Universidad de Chile, Santiago 8370449, Chile*

[4]*Departamento de Física, Facultad de Ciencias, Universidad de Chile, Santiago 7800024, Chile*

[5]*Instituto de Ciencias Básicas, Facultad de Ingeniería y Ciencias, Universidad Diego Portales, Santiago 8370191, Chile*

[6]*Institute of Physics, Pontificia Universidad Católica de Chile, Santiago 7820436, Chile*

[7]*Department of Chemistry and Biochemistry, University of California, Los Angeles, CA 90095, USA*

[8]*California NanoSystems Institute, Los Angeles, CA 90095, USA*

[9]*Center for the Development of Nanoscience and Nanotechnology (CEDENNA), Santiago 9170022, Chile*

[*] sobhit.singh@rutgers.edu

[†] Aldo.Romero@mail.wvu.edu

[‡] fvmunoz@u.uchile.cl

Supplementary Table 1

Supplementary Table I. Listing of superconducting parameters required for the prediction of T_c within isotropic Migdal-Eliashberg theory for some reported 2D phonon-mediated superconductors. This table includes data of effective Coulomb screening parameter μ^*, electronic DOS at the Fermi level $N(\mathrm{E}_F)$ (in states/spin/Ry/cell), logarithmic averaged phonon frequency ω_{log} (in K), total electron-phonon coupling constant λ, and estimated T_c (in K). Experimental T_c values are noted in the table.

Compounds	μ^*	$N(\mathrm{E}_F)$	ω_{log}	λ	T_c	Ref.
B_2C	0.10		315	0.92	19	[1]
CaC_6	0.115		446	0.40	1.4	[2]
LiC_6	0.115		400	0.61	8.1	[2]
LiC_6				0.58 ± 0.05	5.9 [Exp.]	[3]
LiC_6	0.12/0.14/0.16			0.55	7.6/5.9/5.1	[4]
2H-$NbSe_2$				0.75	3.1 [Exp.]	[5]
2H-$NbSe_2$	0.15, 0.16		134, 145	0.84, 0.67	4.5, 2.7	[6,7]
C_6CaC_6					4.0 [Exp.]	[8]
C_6CaC_6	0.207/0.155				6.8/8.1	[9–11]
B(β_{12})	0.10–0.15	8.12	425	0.69	14	[12]
B(α)	0.05	5.85	262	0.52	7	[13]
Borophene	0.10		421	0.79	19	[14]
Borophene	0.10			0.6-1.1	10–20	[15]
Li_2B_7	0.12		463	0.56	6	[16]
$TiSi_4$	0.10			0.59	5.8	[17]
Mo_2C	0.10			0.63	5.9	[18]
Cu-BHT	0.10		51.8	1.16	4.43	[19]
β_0-PC	0.10	7.27	118	1.48	13.4	[20]
tetr-Mo_2B_2	0.10	16.02	345	0.49	4	[21]
tri-Mo_2B_2	0.10	16.81	295	0.30	0.2	[21]
tetr-W_2B_2	0.10	12.46	232	0.69	8	[22]
hex-W_2B_2	0.10	13.60	232	0.43	1.5	[22]
strained-YS	0.10	0.75–1.05	243–100	0.20–0.90	0–6	[22]
B_2O	0.10	5.4	250	0.75	10.3	[23]
bulk MgB_2	0.05	9.8	707	0.73	40	[24]
bulk MgB_2	0.13	9.8		0.61	39	[25]
monolayer MgB_2	0.13	13.1		0.68	20	[25]
monolayer H-MgB_2	0.13	19.2		1.46	67	[26]
$Mg_2B_4C_2$	0.04	12.6	506	1.40	48.1	This work
	0.10				47.2	This work
	0.14				47.0	This work

Supplementary Note 1: Thicker Slabs of $Mg_nB_{2n}C_2$

The most general form of the studied $Mg_2B_4C_2$ monolayer is obtained by replicating the inner layers of MgB_2 shown by the dashed rectangular area in Figure 1(b) of the main text. Thus resulting slab is similar to a MgB_2 slab but with inert surfaces of B-C layers, instead of B-B surfaces in a MgB_2 slab. The calculated band structures of $Mg_nB_{2n}C_2$ for $n = 3, 4$, and 5 are shown in Supplementary Figure 1. As the number of the inner MgB_2 layers increases, the σ subbands create a more MgB_2-like bandstructure (almost independent of k_z in bulk). This is a strong indication of transference of the superconducting properties from the bulk to quasi-2D.

The behavior of the p_z bands is more complicated, with extra degenerate band crossings near the Dirac points at K high symmetry point. These degeneracies are expected as long the inversion and time-reversal symmetry are preserved. The different on-site energy of the C atom is responsible for avoided crossings near the K high symmetry point.

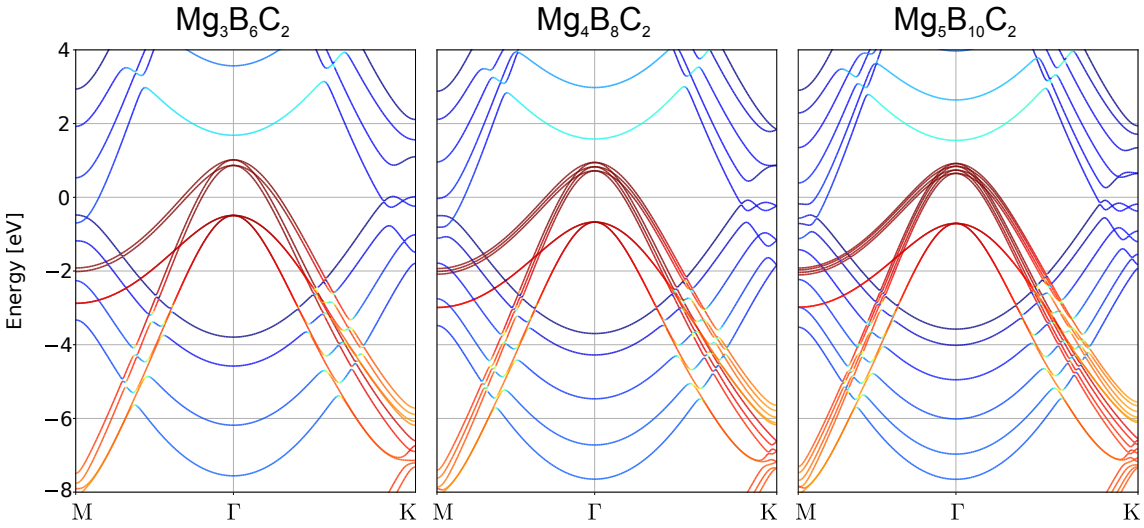

Supplementary Figure 1. Band structures of thicker slabs of $Mg_nB_{2n}C_2$ with preserved inversion symmetry. The $p_{x,y}$ σ orbitals are colored red and the p_z orbitals are blueish.

Supplementary Note 2: Alternative arrangement without inversion symmetry

The studied $Mg_2B_4C_2$ monolayer can have two versions depending upon on the ordering of the boron and carbon atoms in the top and bottom surface layers, as shown in Supplementary Figure 2. $Mg_2B_4C_2$ monolayer preserves the inversion symmetry if the top and bottom layers are made of C-B and B-C (notice the ordering of atoms in unit cell). Whereas, the inversion symmetry is broken if the top and bottom layers are made of B-C and B-C (or both C-B). The inversion symmetric structure, discussed in the main text, is $\sim 5\,\mathrm{meV/f.u.}$ energetically more favorable than the structure with broken inversion symmetry.

Also, if we add a MgB_2 layer to the inversion symmetric $Mg_2B_4C_2$, the resulting system– $Mg_3B_6C_2$– will break the inversion symmetry. In order to preserve this symmetry, we need to interchange the boron and carbon atoms in one B-C layer. The same principle applies for thicker slabs: if the C atoms belong to the same sublattice, the whole system is inversion symmetric (asymmetric) for an odd (even) number of Mg layers.

The lack of inversion symmetry opens a bandgap at the Dirac points, see Supplementary Figure 3, in the same way as an external electric field opens a band gap in bilayer graphene[27]. As the low energy representation (p_z bands) of both systems become equivalent, the analogy with bilayer graphene also implies the emergence of the valley Hall effect if a suitable electric field is applied[28]. The magnitude of the band gap, due to inversion asymmetry, is about 0.8 eV for $Mg_2B_4C_2$ monolayer, and it decreases steadily with increasing slab thickness.

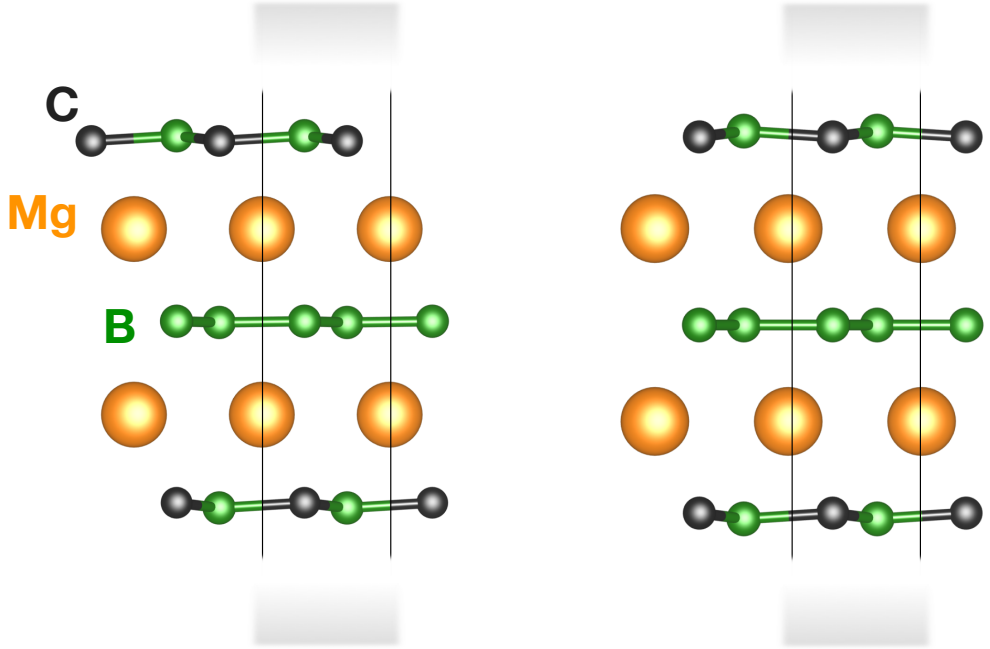

Supplementary Figure 2. Crystal structure. Side view (as viewed from $\vec{\mathbf{b}}$) of $Mg_2B_4C_2$ monolayer with inversion symmetry (left) and without inversion symmetry (right). Mg, B, and C atoms are shown in orange, green, and black, respectively. Solid black lines mark the unit cell boundaries while the shaded grey areas represent vacuum. In the left panel, the in-plane ordering of atoms in the top and bottom layers is C–B–C–B–$\cdots$ and B–C–B–C–$\cdots$, respectively. Whereas, the in-plane ordering of atoms in the right panel is the same (*i.e.*, B-C) for the top and bottom surfaces.

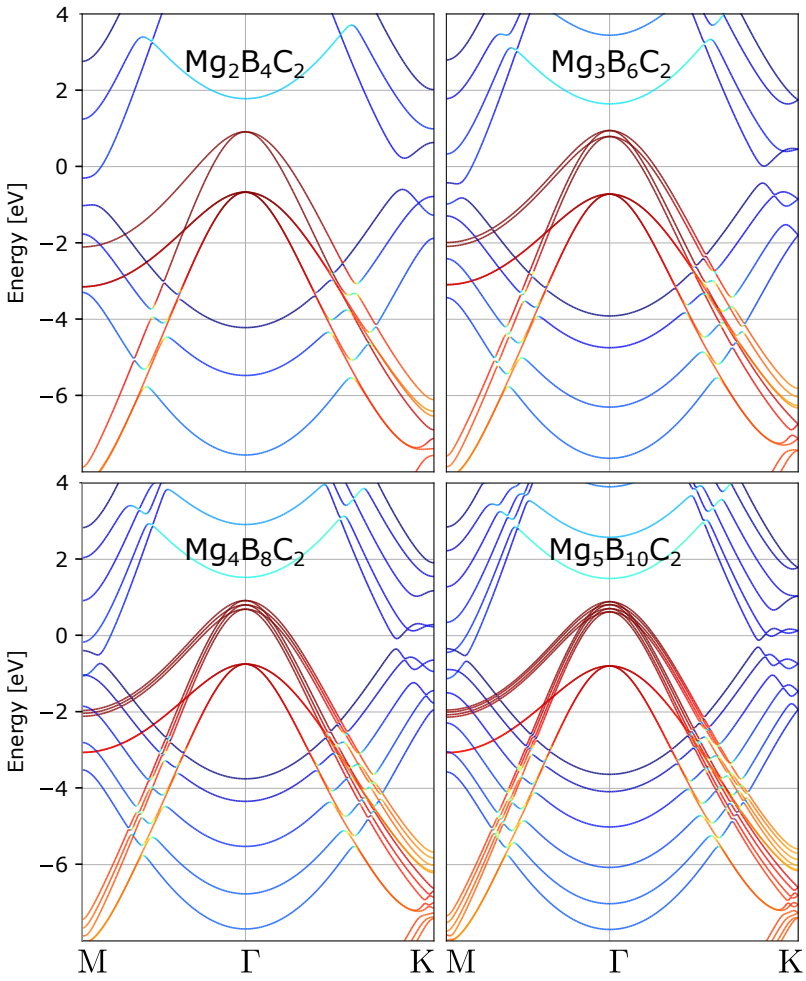

Supplementary Figure 3. Electronic band structures of the thicker slabs of $Mg_nB_{2n}C_2$ with broken inversion symmetry. The $p_{x,y}$ σ orbitals are colored red and the p_z orbitals are blueish.

Supplementary Note 3: Tight-Binding Parametrization

The projection of atomic orbitals on the electronic band structure of $Mg_2B_4C_2$ monolayer is shown in Supplementary Figure 4(a). The accuracy of our Wannier tight-binding parametrization is shown in Supplementary Figure 4(b).

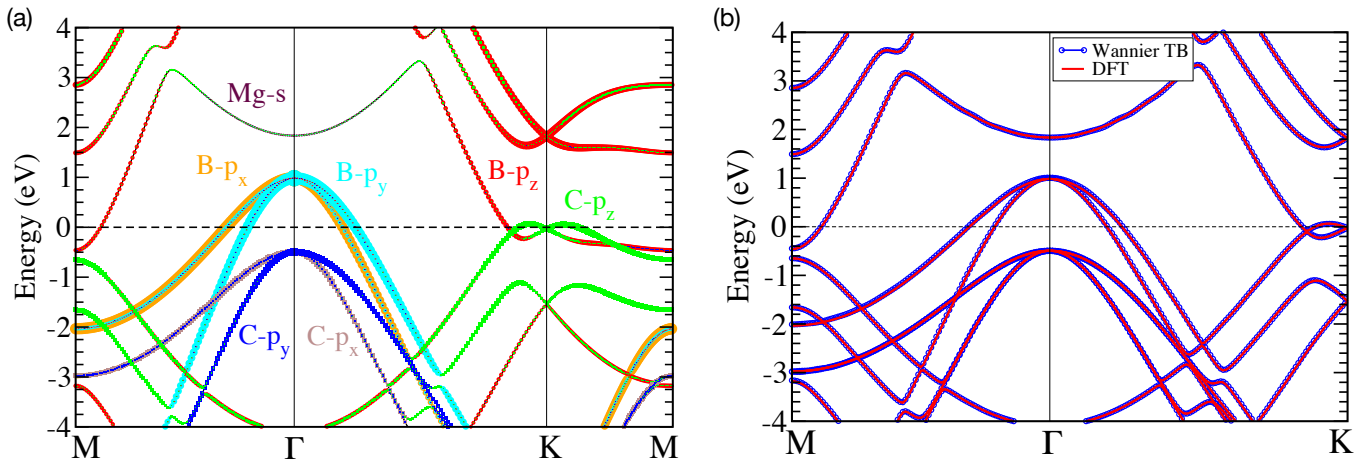

Supplementary Figure 4. (a) Atomic orbitals resolved electronic bandstructure calculated without inclusion of spin-orbit coulping (DFT-PBE) for $Mg_2B_4C_2$ monolayer. (b) Comparison of the DFT bandstructure with the same obtained from Wannier tight-binding (TB) model.

Supplementary Figure 5: Density of States

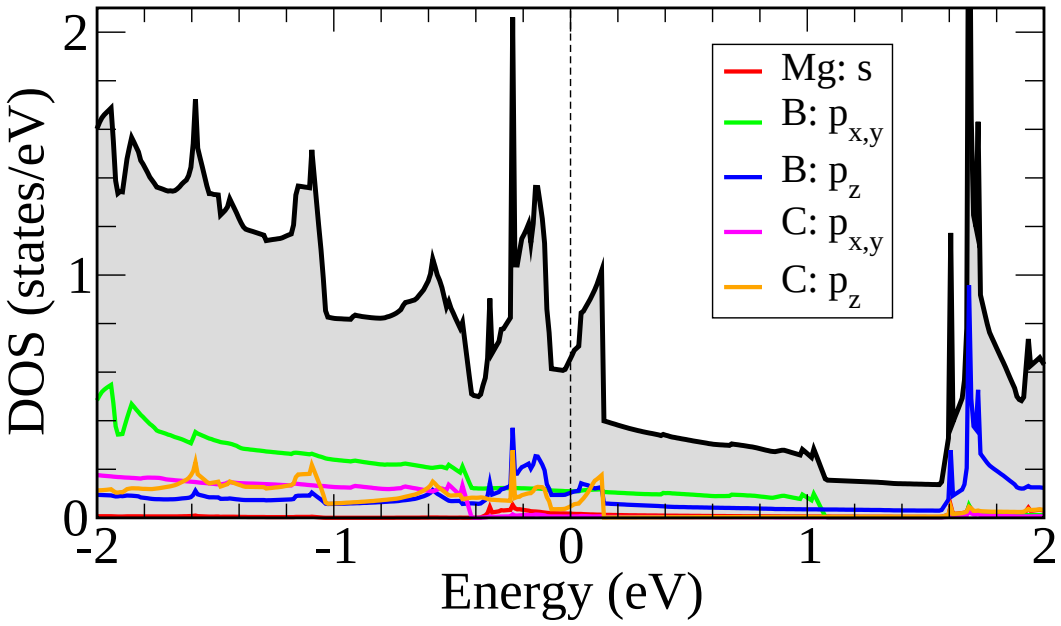

Supplementary Figure 5. The total and partial density of states (DOS) calculated for $Mg_2B_4C_2$ monolayer with inversion symmetry. Black line represents the total DOS, whereas, colored lines represent the partial DOS as defined in the figure legend.

Supplementary Note 4: Elastic Properties

Our elastic constants calculations indicate the elastic and mechanical stability of both inversion-symmetric and inversion-asymmetric $Mg_2B_4C_2$ monolayers. Both monolayers satisfy the Born-Huang mechanical stability conditions for 2D systems[29,30]. We further calculate various elastic moduli defined for 2D systems, as given in Supplementary Table II.

Supplementary Table II. Elastic properties (N/m units) of the $Mg_2B_4C_2$ monolayer with and without inversion-symmetry calculated using DFT-PBE method

	C_{11}	C_{12}	C_{66} = Shear modulus	Layer modulus	Young's modulus	Poisson's ratio
Inversion-symmetric monolayer	396	136	130	266	350	0.34
Inversion-asymmetric monolayer	434	94	170	264	414	0.22

Supplementary Figure 6: Phonons

The calculated phonon spectrum for the $Mg_2B_4C_2$ monolayer with broken inversion symmetry is shown in Supplementary Figure 6. All positive phonon frequencies indicate the dynamical stability of this structure.

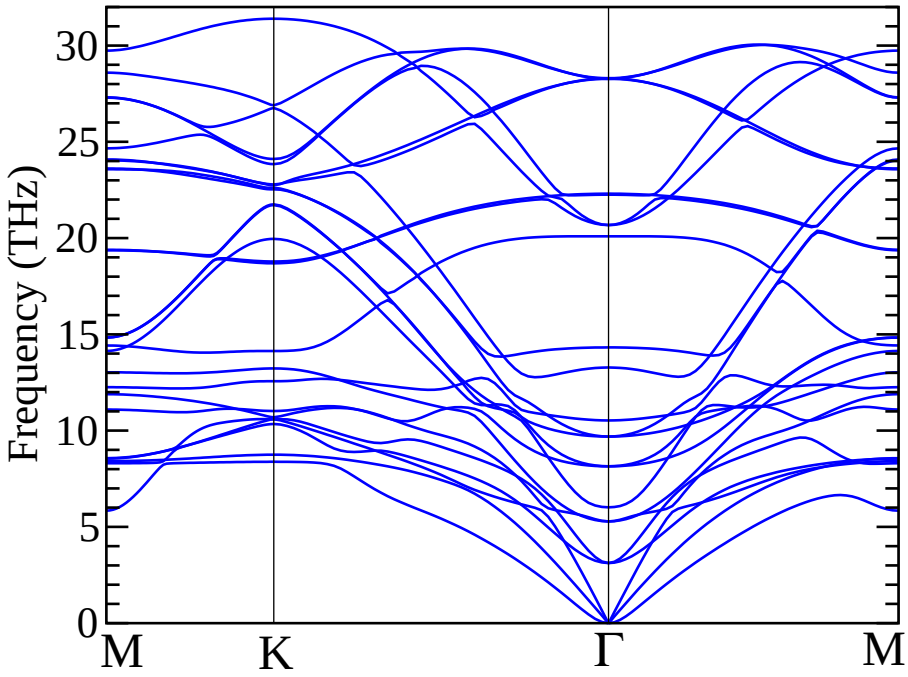

Supplementary Figure 6. Full phonon spectrum calculated using $4 \times 4 \times 1$ supercell along the high symmetry directions of the momentum space of $Mg_2B_4C_2$ monolayer with broken inversion symmetry.

Supplementary Note 5: Exfoliation Energy

To discern if $Mg_2B_4C_2$ would be truly a 2D van der Waal (vdW) material, we built its bulk phase and calculate its exfoliation energy (E_{ex}). For the bulk we considered three different arrangements of the $Mg_2B_4C_2$ layers: (i) a simple vertical stacking or AA, (ii) a Bernal-type stacking AB1, where atoms of different species (B, C) face each other across the vdW gap, and (iii) another Bernal-type stacking AB2, atoms of the same specie face each other across the vdW gap (C–C in one gap, and B–B in the next one).

Supplementary Table III. Calculated exfoliation energy (E_{ex}) for possible bulk phases discussed in the text. The exchange-correlation (XC) functionals are ordered from the one expected to be less accurate to the most accurate for vdW systems.

E_{ex} (meV/Å^2)	AA	AB1	AB2
PBE	0.1	0.1	0.1
SCAN	9.7	10.5	7.9
vdW-DF2	24.8	25.0	22.4
SCAN+rVV10	27.8	29.2	25.8

E_{ex} was calculated for four different approximations of the exchange-correlation term: the Perdew-Burke-Ernzerhof[31] (PBE) GGA approximation, the SCAN[32] meta-GGA, the so-called vdW-DF2 GGA functional[33], and SCAN together with the rVV10 correlation functional (SCAN+rVV10)[34]. It is generally accepted that SCAN+rVV10 is the most accurate approximation within DFT for study of vdW systems; the vdW-DF2 functional also provides a reasonable value of E_{ex}[35].

Mounet *et al.*[36] studied a full set of existing three dimensional materials to search for exfoliable 2D subsystems. They found a threshold of $E_{ex} \approx 35$ meV/Å^2 to define "easily exfoliable" materials. $Mg_2B_4C_2$ lies within this region, hence, it can be regarded as an "easily exfoliable" material.

Supplementary Note 6: When B-C layer is introduced only on one surface

We tested a case in which B-C substitution is done only on one surface of MgB_2 slab, as shown in Supplementary Figure 7(a). Such a substitution resulted in a structure with broken inversion symmetry (space group $p3m1$) having composition $Mg_2B_5C_1$. We fully optimized this structure and computed its phonon spectrum, which is shown in Supplementary Figure 7(b). We note that this structure is dynamically unstable and it is 0.928 eV/atom (DFT-PBE) higher in formation energy compared to that of the original $Mg_2B_4C_2$ monolayer presented in the main draft. Therefore, it is unlikely that $Mg_2B_5C_1$ monolayer would be energetically favored over the $Mg_2B_4C_2$ monolayer presented in this work.

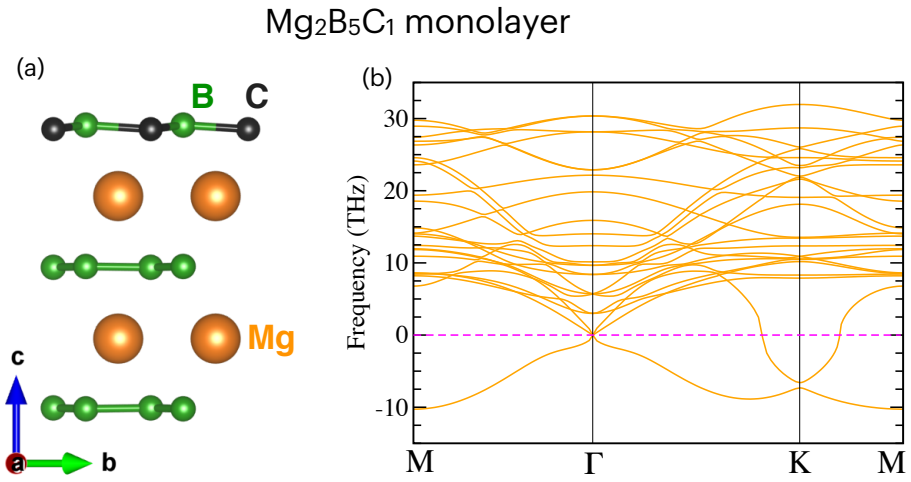

Supplementary Figure 7. (a) Crystal structure, and (b) calculated phonon spectrum of $Mg_2B_5C_1$ monolayer having space group $p3m1$.

Supplementary Table 4: Optimized structural information

Supplementary Table IV. Optimized structural information of the $Mg_2B_4C_2$ inversion-symmetric monolayer (layer group $p\bar{3}m1$, #72) presented in the main draft

Lattice vectors (Å)	x	y	z
a	2.4867	−1.4357	0.00000
b	2.4867	1.4357	0.0000
c	0.0000	0.0000	35.5000

Fractional coordinates	x	y	z
Mg	0.0000	0.0000	0.9492
Mg	0.0000	0.0000	0.0508
B	0.3333	0.3333	0.8981
B	0.3333	0.3333	0.9997
B	0.6666	0.6666	0.0003
B	0.6666	0.6666	0.1019
C	0.6666	0.6666	0.9009
C	0.3333	0.3333	0.0991

Supplementary References

[1] Dai, J., Li, Z., Yang, J. & Hou, J. A first-principles prediction of two-dimensional superconductivity in pristine B_2C single layers. *Nanoscale* **4**, 3032–3035 (2012).

[2] Profeta, G., Calandra, M. & Mauri, F. Phonon-mediated superconductivity in graphene by lithium deposition. *Nat. Phys.* **8**, 131–134 (2012).

[3] Ludbrook, B. M. *et al.* Evidence for superconductivity in Li-decorated monolayer graphene. *Proc. Natl. Acad. Sci.* **112**, 11795–11799 (2015).

[4] Zheng, J.-J. & Margine, E. R. First-principles calculations of the superconducting properties in Li-decorated monolayer graphene within the anisotropic Migdal-Eliashberg formalism. *Phys. Rev. B* **94**, 064509 (2016).

[5] Xi, X. *et al.* Strongly enhanced charge-density-wave order in monolayer NbSe2. *Nature Nanotechnology* **10**, 765–769 (2015).

[6] Lian, C.-S., Si, C. & Duan, W. Unveiling charge-density wave, superconductivity, and their competitive nature in two-dimensional $NbSe_2$. *Nano Letters* **18**, 2924–2929 (2018).

[7] Zheng, F. & Feng, J. Electron-phonon coupling and the coexistence of superconductivity and charge-density wave in monolayer $NbSe_2$. *Phys. Rev. B* **99**, 161119 (2019).

[8] Ichinokura, S., Sugawara, K., Takayama, A., Takahashi, T. & Hasegawa, S. Superconducting calcium-intercalated bilayer graphene. *ACS Nano* **10**, 2761–2765 (2016).

[9] Margine, E. R., Lambert, H. & Giustino, F. Electron-phonon interaction and pairing mechanism in superconducting Ca-intercalated bilayer graphene. *Scientific Reports* **6**, 21414 (2016).

[10] Mazin, I. & Balatsky, A. Superconductivity in ca-intercalated bilayer graphene. *Philosophical Magazine Letters* **90**, 731–738 (2010).

[11] Jishi, R., Guzman, D. & Alyahyaei, H. Theoretical investigation of two-dimensional superconductivity in intercalated graphene layers. *Adv. Studies Theor. Phys.* **5**, 703 – 716 (2011).

[12] Cheng, C. *et al.* Suppressed superconductivity in substrate-supported 12 borophene by tensile strain and electron doping. *2D Materials* **4**, 025032 (2017).

[13] Zhao, Y., Zeng, S. & Ni, J. Superconductivity in two-dimensional boron allotropes. *Phys. Rev. B* **93**, 014502 (2016).

[14] Xiao, R. C. *et al.* Enhanced superconductivity by strain and carrier-doping in borophene: A first principles prediction. *Applied Physics Letters* **109**, 122604 (2016).

[15] Penev, E. S., Kutana, A. & Yakobson, B. I. Can two-dimensional boron superconduct? *Nano Lett.* **16**, 2522–2526 (2016).

[16] Wu, C. *et al.* Lithium–boron (Li–B) monolayers: First-principles cluster expansion and possible two-dimensional superconductivity. *ACS Applied Materials & Interfaces* **8**, 2526–2532 (2016).

[17] Wu, Q. *et al.* Versatile titanium silicide monolayers with prominent ferromagnetic, catalytic, and superconducting properties: Theoretical prediction. *J. Phys. Chem. Lett.* **7**, 3723–3729 (2016).

[18] Zhang, J.-J. & Dong, S. Superconductivity of monolayer Mo_2C: The key role of functional groups. *J. Chem. Phys.* **146**, 034705 (2017).

[19] Zhang, X., Zhou, Y., Cui, B., Zhao, M. & Liu, F. Theoretical discovery of a superconducting two-dimensional metal–organic framework. *Nano Letters* **17**, 6166–6170 (2017).

[20] Wang, B.-T. *et al.* Superconductivity in two-dimensional phosphorus carbide (β_0-PC). *Phys. Chem. Chem. Phys.* **20**, 12362–12367 (2018).

[21] Yan, L. *et al.* Prediction of phonon-mediated superconductivity in two-dimensional Mo_2B_2. *J. Mater. Chem. C* **7**, 2589–2595 (2019).

[22] Yan, L. *et al.* Novel structures of two-dimensional tungsten boride and their superconductivity. *Phys. Chem. Chem. Phys.* **21**, 15327–15338 (2019).

[23] Yan, L. *et al.* Theoretical dissection of superconductivity in two-dimensional honeycomb borophene oxide B_2O crystal with a high stability. *npj Computational Materials* **6**, 94 (2020).

[24] Bohnen, K.-P., Heid, R. & Renker, B. Phonon dispersion and electron-phonon coupling in MgB_2 and AlB_2. *Phys. Rev. Lett.* **86**, 5771–5774 (2001).

[25] Bekaert, J., Aperis, A., Partoens, B., Oppeneer, P. M. & Milošević, M. V. Evolution of multigap superconductivity in the atomically thin limit: Strain-enhanced three-gap superconductivity in monolayer MgB_2. *Phys. Rev. B* **96**, 094510 (2017).

[26] Bekaert, J., Petrov, M., Aperis, A., Oppeneer, P. M. & Milošević, M. V. Hydrogen-induced high-temperature superconductivity in two-dimensional materials: The example of hydrogenated monolayer mgb_2. *Phys. Rev. Lett.* **123**, 077001 (2019).

[27] McCann, E. Asymmetry gap in the electronic band structure of bilayer graphene. *Phys. Rev. B* **74**, 161403 (2006).

[28] Sui, M. *et al.* Gate-tunable topological valley transport in bilayer graphene. *Nat. Phys.* **11**, 1027 (2015).

[29] Born, M. & Huang, K. *Dynamical theory of crystal lattices* (Clarendon press, 1954).

[30] Mavko, G., Mukerji, T. & Dvorkin, J. *The rock physics handbook* (Cambridge university press, 2020).

[31] Perdew, J. P., Burke, K. & Ernzerhof, M. Generalized gradient approximation made simple. *Phys. Rev. Lett.* **77**, 3865–3868 (1996).

[32] Sun, J., Ruzsinszky, A. & Perdew, J. P. Strongly constrained and appropriately normed semilocal density functional. *Phys. Rev. Lett.* **115**, 036402 (2015).

[33] Lee, K., Murray, E. D., Kong, L., Lundqvist, B. I. & Langreth, D. C. Higher-accuracy van der waals density functional. *Phys. Rev. B* **82**, 081101 (2010).

[34] Peng, H., Yang, Z.-H., Perdew, J. P. & Sun, J. Versatile van der waals density functional based on a meta-generalized gradient approximation. *Phys. Rev. X* **6**, 041005 (2016).

[35] Tran, F., Kalantari, L., Traoré, B., Rocquefelte, X. & Blaha, P. Nonlocal van der waals functionals for solids: Choosing an appropriate one. *Phys. Rev. Materials* **3**, 063602 (2019).

[36] Mounet, N. *et al.* Two-dimensional materials from high-throughput computational exfoliation of experimentally known compounds. *Nature Nanotechnology* **13**, 246–252 (2018).